EES Catalysis

ROYAL SOCIETY OF CHEMISTRY

COMMUNICATION

View Article Online
View Journal | View Issue

Check for updates

Cite this: *EES Catal.*, 2025, 3, 259

Received 19th November 2024,
Accepted 26th December 2024

DOI: 10.1039/d4ey00252k

rsc.li/eescatalysis

Integrating oxophilic and protophilic properties in a multivalent Co_9S_8@$CoMoP_x$ electrode to boost alkaline hydrogen evolution†

Xijie Chen,[a] Fengming Zhang,[a] Xiao Wang,[a] Fangming Liu,[a] Jinhan Li,[a]
Meng Yu *[a] and Fangyi Cheng *[ab]

The alkaline hydrogen evolution reaction (HER) is plagued by intricate interfacial reactions involving the dissociation of interfacial H_2O molecules and adsorption/desorption of H_{ads}/OH_{ads} species, which impede the practical application of water electrolysis. Herein, a self-supported Co_9S_8@$CoMoP_x$ electrode with a nanosheet cluster morphology was developed using a stepwise electrodeposition method for an efficient electrocatalytic HER. Benefiting from the coexistence of multivalent metal sites, the Co_9S_8@$CoMoP_x$ electrode integrated both oxophilic and protophilic properties to facilitate the cracking of molecular H_2O and subsequent hydrogen generation. As a result, the obtained Co_9S_8@$CoMoP_x$ electrode exhibited superior alkaline HER activities, delivering an overpotential of 226 mV at −500 mA cm^{-2} with a low attenuation rate of 11 μV h^{-1} after 1000 h. An anion-exchange membrane water electrolysis device was then assembled by matching the Co_9S_8@$CoMoP_x$ cathode with an NiFe-based anode to demonstrate its industrial application potential. This work emphasizes the significance of constructing multivalent metal sites to simultaneously achieve oxophilicity and protophilicity, providing a guideline for the rational design of heterostructure electrocatalysts for efficient energy conversion.

Broader context

Sustainable anion-exchange membrane water electrolysis (AEMWE) is recognized as a promising candidate to mitigate the current carbon emission issues and realize the future hydrogen economy. However, as the cathodic reaction, the hydrogen evolution reaction (HER) is plagued by the dissociation of interfacial H_2O molecules and the adsorption/desorption of H_{ads}/OH_{ads} species, which result in sluggish water dissociation and high energy loss in green hydrogen production. In this work, we report a double-layered Co_9S_8@$CoMoP_x$ self-supported electrode with multivalent active sites to address intricate interfacial reactions in the alkaline HER. Multivalent metal sites on the surface endow the Co_9S_8@$CoMoP_x$ electrocatalyst with both low-valence protophilic sites and high-valence oxophilic sites, thus accelerating catalytic kinetics and delivering low overpotentials of 41 and 226 mV at current densities of −10 and −500 mA cm^{-2}. Meanwhile, $Co(OH)_x$ on the surface can impede the leaching of MoO_4^{2-} ions through electrostatic interaction and enhance catalytic stability for long-term operation (1000 h at −500 mA cm^{-2}). This work not only emphasizes the significance of constructing composite electrocatalysts with multivalent metal sites to simultaneously achieve oxophilicity and protophilicity but also provides a reference for the precise customization of self-supported heterostructure electrocatalysts for efficient energy conversion.

Introduction

Alkaline anion-exchange membrane water electrolysis (AEMWE) holds great promise for fossil-free and sustainable hydrogen production with intermittent electricity.[1–3] However, the proton-deficient environment of AEMWE represents an obstacle to the cathodic hydrogen evolution reaction (HER), which limits the overall energy efficiency and large-scale application of AEMWE.[4–6] The alkaline HER usually follows the Volmer–Heyrovsky or Volmer–Tafel mechanism, in which the water dissociation step is the essential path of the reaction.[7–9] Unlike the acidic environment with abundant hydrated protons (H_3O^+), adsorbed hydrogens (H_{ads}) are provided by the initial water dissociation step (Volmer step: $H_2O + e^- \rightarrow H_{ads} + OH^-$) on the electrocatalyst under alkaline conditions.[10,11] The activation and dissociation of H_2O molecules not only require additional energy to break strong H–OH bonds but also involve the adsorption and desorption of H_{ads} and OH_{ads} species, resulting in a sluggish reaction rate and

---

[a] Key Laboratory of Advanced Energy Materials Chemistry (Ministry of Education), Engineering Research Center of High-efficiency Energy Storage (Ministry of Education), College of Chemistry, Nankai University, Tianjin 300071, China. E-mail: nkyu2023@nankai.edu.cn, fycheng@nankai.edu.cn

[b] Haihe Laboratory of Sustainable Chemical Transformations, Tianjin 300192, China

† Electronic supplementary information (ESI) available. See DOI: https://doi.org/10.1039/d4ey00252k

unsatisfactory electrocatalytic efficiency.[12–14] Accordingly, innovative electrocatalyst design strategies are desirable to conquer this limitation for achieving an efficient alkaline HER.

To overcome this kinetic barrier, interface engineering strategies conducted on heterogeneous catalysts have been critically explored.[15,16] For example, Pt nanoparticles were loaded onto MgO nanosheets with oxygen vacancies, whereby MgO could promote H_2O dissociation and H_3O^+ accumulation around $Pt^{\delta-}$ sites to form an acid-like local microenvironment, which accelerated the kinetics of the alkaline HER.[17] Moreover, CeO_2 and CoS_2 materials were coupled to form a heterostructure, in which CeO_2 provided strong acidic Ce sites to promote the adsorption and dissociation of water, while CoS_2 offered weakly basic S sites for the surface transfer of H_{ads} and subsequent H_2 evolution.[18] Although the above heterostructure electrocatalysts delivered impressive alkaline HER performances, their synergistic effect was trapped at the limited interface between the different components. For overcoming this, constructing electrocatalysts with mixed multivalent metal ions would be beneficial for integrating multifunctional reaction sites with proper H_2O dissociation or H_{ads}/OH_{ads} adsorption ability at the atomic level. Besides, the combination of a surface protective layer and internal active material with a partially leachable component can improve the stability without having a significant impact on catalytic activity.[19,20] Therefore, a heterostructure electrocatalyst with the coexistence of a protective layer and multivalent active sites could be expected to drive stable cathodic HER processes in alkaline conditions.

In this research, a double-layered Co_9S_8@$CoMoP_x$ self-supported cathode with multivalent active sites was designed and fabricated by a continuous cathodic layer-by-layer assembly method. Owing to the introduction of the Mo element, the inherent electronic structure of Co_9S_8@$CoMoP_x$ was modulated, which contributed to the existence of multivalent Co metal sites on the surface at the atomic level and endowed the Co_9S_8@$CoMoP_x$ electrode with both low-valence protophilic sites and high-valence oxophilic sites. Detailed electrochemical investigations were performed and demonstrated that Co_9S_8@$CoMoP_x$ delivered excellent catalytic performance with a low overpotential of 226 mV to reach -500 mA cm^{-2} and long-term stability for 1000 h by inhibiting MoO_4^{2-} leaching through an electrostatic anchoring effect of the high-valence sites in the Co_9S_8 layer. To explore the prospect of practical industrial applications, the Co_9S_8@$CoMoP_x$ cathode was also scaled-up and assembled into an AEMWE device coupled with a Ni_3S_2@$NiFeP_x$ anode. The results in the present study highlight the significance of multivalent active sites and a protective layer for realizing an efficient and stable alkaline HER process.

Results and discussions

As schematically presented in Fig. 1a, the Co_9S_8@$CoMoP_x$ electrode was fabricated by a continuous two-step electrodeposition method on conductive Ni foam (NF). $CoMoP_x$ and Co_9S_8 electrodes were prepared by similar one-step cathodic depositions. Compared to the plane surface of the blank NF substrate (Fig. S1, ESI†), the $CoMoP_x$ electrode exhibited a nanosphere morphology with aggregated nanoparticles (Fig. 1b and Fig. S2a–c, ESI†), while Co_9S_8 showed an almost nanosheets morphology (Fig. 1c and Fig. S3a–c, ESI†). Meanwhile, Co_9S_8 deposited on the $CoMoP_x$ surface basically retained the original morphology of stacked-nanosheets (Fig. 1d and Fig. S4a–c, ESI†). Energy dispersive spectrometry (EDS) analysis demonstrated the uniform distribution of elements in $CoMoP_x$ (Fig. S2d, ESI†), Co_9S_8 (Fig. S3d, ESI†), and Co_9S_8@$CoMoP_x$ (Fig. S4d, ESI†). To optimize the deposition parameters of the electrocatalyst, $CoMoP_x$ electrodes prepared with different deposition times were characterized by scanning electron microscopy (SEM) (Fig. S5, ESI†). As the deposition time was extended, the surface roughness increased accordingly, and the $CoMoP_x$ layer appeared to show cracks at the edge of the NF at 20 min (Fig. S5h, ESI†). These fractures induced by internal mechanical stress and bubble release could easily cause catalyst stripping from the NF substrate and a subsequent decline in activity. Therefore, the $CoMoP_x$ catalyst prepared with a 15 min deposition time was selected as the bottom layer. After that, Co_9S_8 with the nanosheets morphology was loaded on $CoMoP_x$ (Fig. S6, ESI†). When the deposition time of the surface layer was only 1 min, Co_9S_8 could not completely cover the underlying $CoMoP_x$ layer (Fig. S6b, ESI†). Further prolonging the deposition time of Co_9S_8, the surface roughness evidently increased. However, as expected, crevices occurred at the electrode surface after 4 min of Co_9S_8 deposition due to the excessive coating thickness (Fig. S6h, ESI†).

In addition, the optimized deposition times of the bottom and surface layer were further investigated by considering the electrochemical performance. As depicted in Fig. S7a (ESI†), when the deposition time of the $CoMoP_x$ layer was 15 min, the double-layered electrode showed the best HER performance. For the top Co_9S_8 layer, 3 min was determined to be an appropriate deposition time to ensure full coverage with a negligible effect on the electrocatalytic activity (Fig. S7b, ESI†). The cross-sectional SEM image of the Co_9S_8@$CoMoP_x$ electrode, prepared by 15 min and 3 min depositions of the $CoMoP_x$ bottom layer and Co_9S_8 surface layer, verified the two-layered structure of the composite (Fig. 1e). Considering the difficulty in distinguishing the signals of Mo and S in the SEM element mapping due to the closely located characteristic peaks of Mo L_α (2.29 keV) and S K_α (2.3 keV), the signal for P was used to identify the bottom and surface layers. According to Fig. S8 (ESI†), the P element was mainly distributed at the bottom, confirming the inner and outer layers were $CoMoP_x$ and Co_9S_8. Besides, element line scanning following the direction of the arrow in Fig. 1e was conducted (Fig. 1f). It was found that the signal for P gradually increased after about 0.65 μm, implying that the thicknesses of the surface Co_9S_8 and bottom $CoMoP_x$ were ∼0.65 μm and ∼0.6 μm, respectively.

Transmission electron microscopy (TEM) images and selected area electron diffraction (SAED) patterns were obtained and confirmed the amorphous and polycrystalline structures of $CoMoP_x$ (Fig. S9, ESI†) and Co_9S_8 (Fig. S10, ESI†), respectively. The related high-resolution transmission electron microscopy

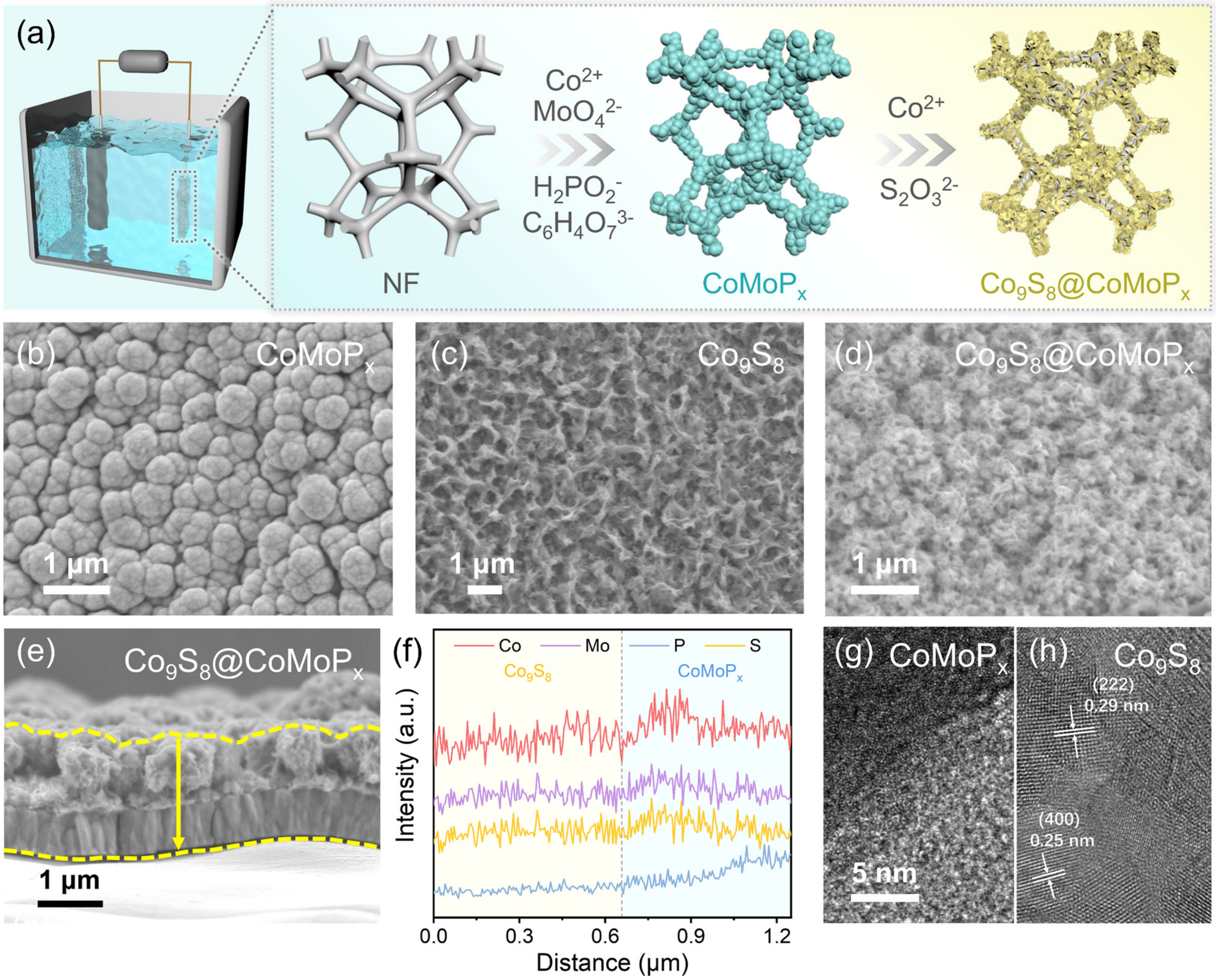

Fig. 1 (a) Schematic of the synthesis route for the Co_9S_8@$CoMoP_x$ electrode. $CoMoP_x$ stands for amorphous cobalt–molybdenum-based phosphide. Surface SEM images of (b) $CoMoP_x$, (c) Co_9S_8 and (d) Co_9S_8@$CoMoP_x$ electrodes. (e) Cross-sectional SEM image of Co_9S_8@$CoMoP_x$ and corresponding (f) elemental line scanning following the arrow in Fig. 1(e). Related high-resolution transmission electron microscopy (HRTEM) images for (g) $CoMoP_x$ and (h) Co_9S_8.

(HRTEM) images in Fig. 1g showed no evident crystal structure for $CoMoP_x$ and obvious lattice fringe spacings of 0.29 and 0.25 nm, corresponding to the (222) and (400) planes of Co_9S_8.[21,22] Moreover, the phase of Co_9S_8 was also examined by X-ray diffraction (XRD) (Fig. S11, ESI†), which gave consistent results with the TEM results.[23,24] Inductively coupled plasma-optical emission spectrometry (ICP-OES) was performed and the results showed that the Co/Mo ratio in the Co_9S_8@$CoMoP_x$ double-layered composite was about 5 : 1 (Table S1, ESI†).

According to the polarization curves in Fig. 2a and Fig. S12, S13, ESI,† Co_9S_8@$CoMoP_x$ demonstrated superior HER performance (41/226 mV@−10/500 mA cm^{-2}) than CoP (188/374 mV@−10/500 mA cm^{-2}), Co_9S_8 (445 mV@−10 mA cm^{-2}), and almost similar to the single-layer $CoMoP_x$ electrode (38/212 mV@−10/500 mA cm^{-2}). The corresponding Tafel slope values of Co_9S_8@$CoMoP_x$ and $CoMoP_x$ were 82.3 and 78.7mV dec^{-1}, which were lower than those for CoP (87.0 mV dec^{-1}) and Co_9S_8 (107.1 mV dec^{-1}) without Mo (Fig. 2b), manifesting the accelerated HER kinetics.[25–27] Electrochemical impedance spectroscopy (EIS) measurements were performed for Co_9S_8@$CoMoP_x$ at −0.1 V *vs.* RHE and showed there was a rapid charge-transfer rate at the electrode–electrolyte interface (Fig. 2c). Meanwhile, operando EIS was also carried out to determine the electron-transfer resistance and reaction kinetics during the HER process. As displayed in Fig. S14 (ESI†), the R_{ct} values of Co_9S_8@$CoMoP_x$ and $CoMoP_x$ were obviously smaller than those of CoP and Co_9S_8 under the same overpotential, illustrating that greater charges were involved in the Faraday reaction on the Co_9S_8@$CoMoP_x$ and $CoMoP_x$ surfaces instead of being stored at the interface.[28,29] Similarly, the phase angles of Co_9S_8@$CoMoP_x$ and $CoMoP_x$ decreased more rapidly (Fig. S15, ESI†), further confirming the accelerated charge-transfer process.[30,31] The C_{dl} value of the Co_9S_8@$CoMoP_x$ electrode was higher than that of other single-layer electrodes (Fig. S16, ESI† and Fig. 2d), implying the double-layered composite fabricated by the two-step layer-by-layer

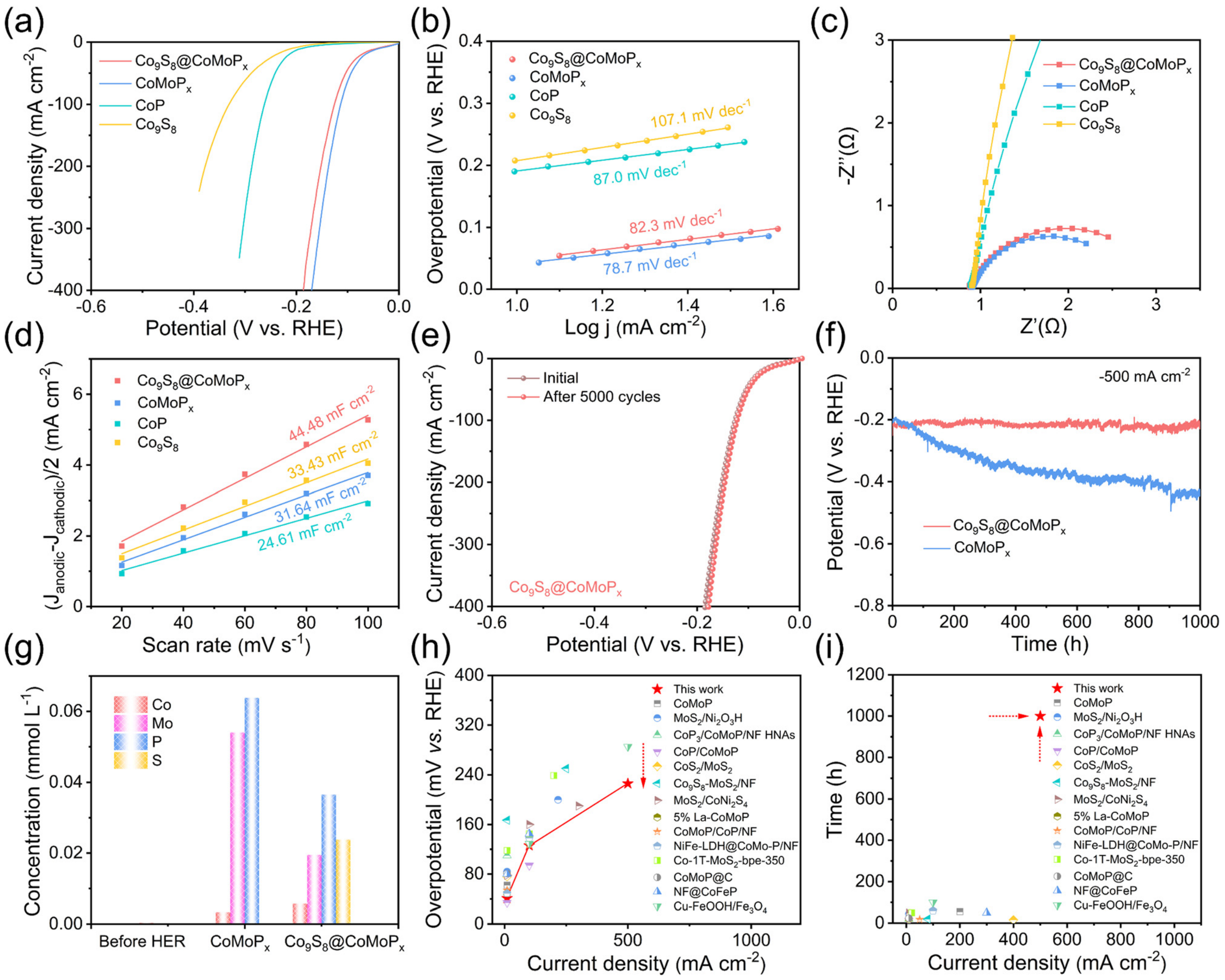

Fig. 2 (a) LSV curves of different electrodes in 1.0 mol L^{-1} KOH with 95% iR-compensation and (b) the corresponding Tafel slopes. (c) Nyquist plots of electrocatalysts measured at −0.1 V (*vs.* RHE) and (d) double-layer capacitances. (e) Accelerated duration test of $Co_9S_8@CoMoP_x$ at a 50 mV s^{-1} scan rate. (f) Chronopotentiometry curves of $Co_9S_8@CoMoP_x$ and $CoMoP_x$ at −500 mA cm^{-2}. (g) Inductively coupled plasma-optical emission spectrometry (ICP-OES) results of the electrolyte after the HER chronopotentiometry tests. The detailed data are listed in Table S2 (ESI†). (h) HER performance and (i) stability comparison of $Co_9S_8@CoMoP_x$ with CoMoP-based catalysts and some other HER catalysts reported in the literature, with the detailed information summarized in Table S3 (ESI†).

cathodic deposition endowed the electrode with a rougher surface and more active sites.

To further evaluate the catalytic stability, accelerated duration tests and chronopotentiometry measurements were performed. As presented in Fig. 2e, the polarization curve of $Co_9S_8@CoMoP_x$ after 5000 cyclic voltammetry (CV) cycles almost overlapped with the original linear sweep voltammetry (LSV) curve. The attenuation of $Co_9S_8@CoMoP_x$ during the accelerated duration test at −100 mA cm^{-2} was only 4 mV, while that for the $CoMoP_x$ electrode was 30 mV (Fig. S17, ESI†), verifying the superior cycling stability of $Co_9S_8@CoMoP_x$. According to the chronopotentiometry test results (Fig. 2f), although the initial HER performance of $CoMoP_x$ was slightly better than that of $Co_9S_8@CoMoP_x$, the catalytic activity seriously declined during continuous operation. In contrast, $Co_9S_8@CoMoP_x$ showed impressive operation stability at −500 mA cm^{-2} for 1000 h with a low attenuation rate of 11 μV h^{-1}. In addition, ICP-OES was applied to analyse the origin of the difference in stability between $Co_9S_8@CoMoP_x$ and $CoMoP_x$ by measuring the dissolved metal contents in the electrolyte after hydrogen evolution (Fig. 2g). A lower Mo content was observed in the electrolyte for $Co_9S_8@CoMoP_x$ after the HER than with the single-layer $CoMoP_x$. The above experiments firmly prove that the polycrystalline Co_9S_8 layer prolonged the operation life of the electrocatalyst by inhibiting the dissolution of Mo sites in the inner $CoMoP_x$ layer. Besides, the microstructure morphology of the $Co_9S_8@CoMoP_x$ electrode could be well-retained with robust features under abundant hydrogen gas evolution (Fig. S18, ESI†). Compared with some other recently reported $CoMoP_x$-based electrocatalysts, the $Co_9S_8@CoMoP_x$ electrode with adjacent oxophilic and protophilic sites demonstrated both impressive HER activity and stability, especially under a larger current density, as shown in Fig. 2h and i.

Next, X-ray photoelectron spectroscopy (XPS) was carried out to probe the chemical composition and elemental valence state of the electrode before and after reaction. The Co 2p spectrum of $CoMoP_x$ displayed signals for Co^0 (∼777.8 and ∼792.8 eV), Co^{3+} (∼781.0 and ∼796.5 eV), Co^{2+} (∼782.5 and ∼798.0 eV), and satellite peaks (∼786.2 and ∼802.8 eV) (Fig. S19a, ESI†).[32,33] The Mo 3d spectrum was divided into four components: Mo^0 (∼227.4 and ∼230.5 eV), Mo^{4+} (∼228.5 and ∼231.6 eV), Mo^{5+} (∼230.3 and ∼233.4 eV), and Mo^{6+} (∼232.1 and ∼235.2 eV) (Fig. S19b, ESI†).[32,34] The P 2p profile presented two peaks at 129.1 and 133.2 eV (Fig. S19c, ESI†), attributed to the characteristic peaks of M–P (M stands for transition metal) and P–O signals, respectively.[35] The Co 2p pattern of Co_9S_8 illustrated the predominant +2 and +3 valence states for the Co element in Co_9S_8 (Fig. S20a, ESI†). The non-metallic S 2p spectrum presented two peaks at ∼163.0 and ∼168.6 eV, which were attributed to M–S and S–O peaks, respectively (Fig. S20b, ESI†).[36] As for Co_9S_8@$CoMoP_x$, according to the Co 2p spectrum (Fig. 3a) of Co_9S_8@$CoMoP_x$ before the chronopotentiometry test, characteristic peaks at 796.5 eV (Co $2p_{1/2}$) and 780.7 eV (Co $2p_{3/2}$), along with two satellite peaks at 803.0 and 785.8 eV could be observed, indicating the presence of Co^{2+} and Co^{3+}. After the chronopotentiometry test, the Co element in the Co_9S_8@$CoMoP_x$ composite became more multivalent with the coexistence of 0, +2, and +3 chemical states (Fig. 3a). While the Mo element mainly existed in a +6 valence state (MoO_4^{2-}) on the surface after reaction (Fig. 3b).[34] Meanwhile, no significant peak was observed in the P 2p diagram after the HER (Fig. 3c) due to the element leaching, as the thick outer layer of Co_9S_8 may block the XPS signal of the underlying $CoMoP_x$ layer. To further rigorously support this speculation, we collected XPS depth profiling of the reacted Co_9S_8@$CoMoP_x$ using the Ar^+ ion, which verified that the P content increased with the etching thickness (Fig. S21, ESI†).

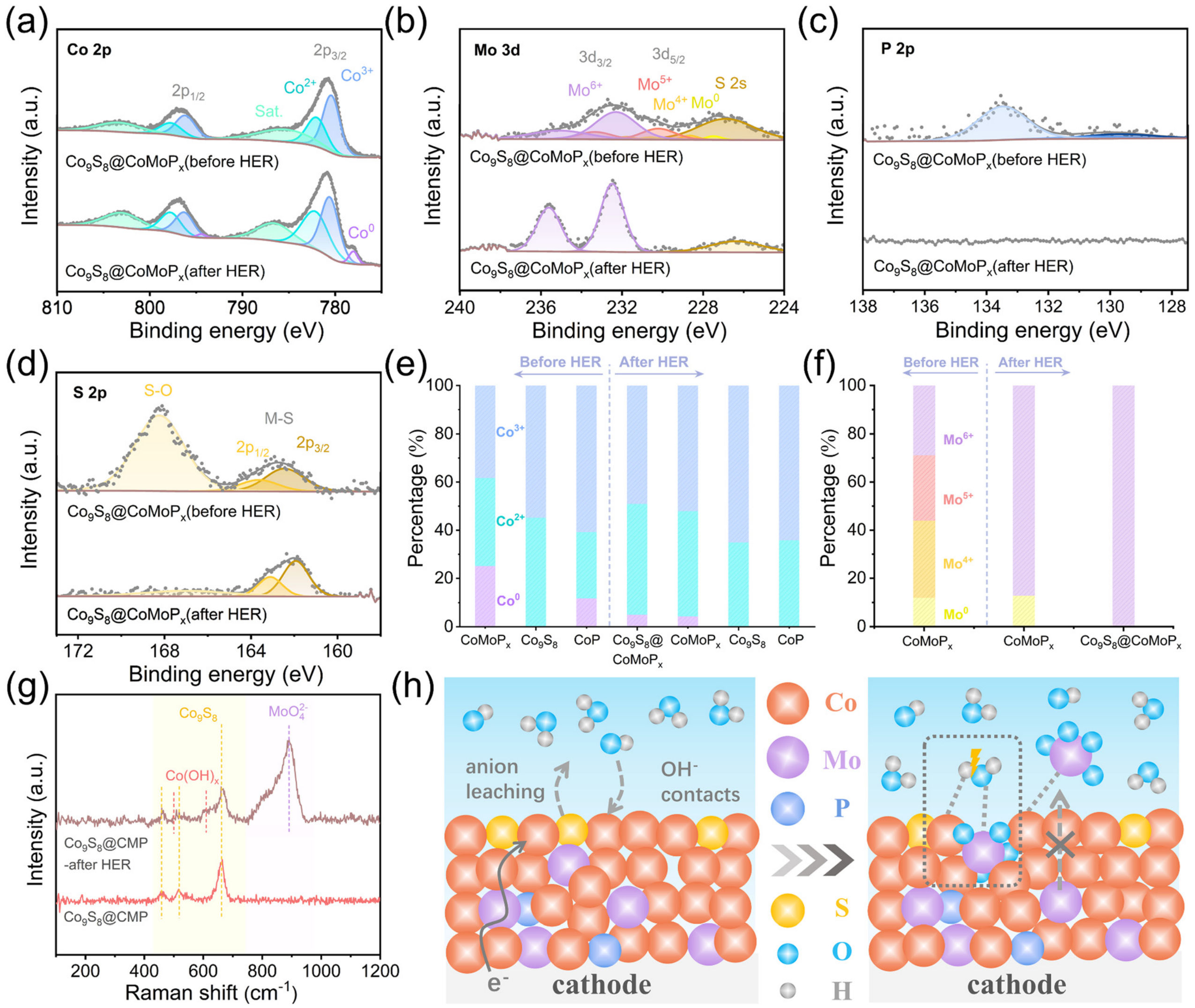

Fig. 3 High-resolution XPS spectra of (a) Co 2p, (b) Mo 3d, (c) P 2p, and (d) S 2p for Co_9S_8@$CoMoP_x$ before and after the HER test. Valence states distribution in XPS spectra of (e) Co 2p and (f) Mo 3d for the above electrodes before and after the HER process. (g) Raman spectra of Co_9S_8@$CoMoP_x$ before and after the HER process. (h) Schematic illustration of the evolution on the Co_9S_8@$CoMoP_x$ surface during the HER process.

Moreover, the content of the surface S element decreased and M–S was the dominant state after the HER (Fig. 3d). To further investigate the reason for the coexistence of multiple Co valence states, the XPS spectra of the electrodes with ($CoMoP_x$) and without Mo (Co_9S_8 and CoP) after hydrogen evolution were also collected. After the HER reaction, the Co 2p spectrum of $CoMoP_x$ also displayed the feature with multivalent Co containing 0, +2, and +3 valence states (Fig. S19d, ESI†), while the Mo 2p spectrum showed signals for Mo^0 and Mo^{6+} (Fig. S19e, ESI†), in which Mo^{6+} was the dominant state (MoO_4^{2-}). In contrast, the Co 2p spectrum of Co_9S_8 after the HER contained only the signal peaks for Co^{2+} and Co^{3+} (Fig. S20c, ESI†), while the S 2p spectrum could be divided into M–S and S–O peaks (Fig. S20d, ESI†). Besides, the Co 2p spectrum for CoP exhibited signal peaks for Co^0, Co^{2+}, and Co^{3+} (Fig. S22a, ESI†). Compared with the Co 2p spectrum of CoP before the HER, $CoMoP_x$ with the Mo component possessed a higher proportion of Co^0, manifesting a possible electronic regulation effect between the Co and Mo atoms. Moreover, the Co ions with multivalent states in the Co 2p spectrum for CoP before the HER turned into a narrower valence distribution of Co^{2+} and Co^{3+} after the reaction (Fig. S22c, ESI†). The P 2p spectra of CoP demonstrated a decrease in P element near the surface (Fig. S22d, ESI†).

The valence states distribution of Co and Mo for the obtained electrocatalysts before and after HER progress was summarized in Fig. 3e and f. The Co element in Co_9S_8@$CoMoP_x$ and $CoMoP_x$ containing Mo components showed the coexistence of multivalent states, including 0, +2, and +3, while that of Co_9S_8 and CoP without the Mo element predominantly showed the +2 and +3 valence states after the HER. As the Pourbaix diagram in aqueous solution depicts, the Mo element mainly existed as Mo^{6+} (MoO_4^{2-}) on the surface of Co_9S_8@$CoMoP_x$ due to the reduction potential of MoO_4^{2-} being lower than the hydrogen evolution potential in alkaline conditions (Fig. 3f).[37] At this point, the coexistence of multivalent states of the Co element could be attributed to two points: on the one hand, abundant OH^- diffusing from the bulk solution or generated by interfacial H_2O dissociation will adhere to the catalyst surface, and then promote the surface hydroxylation to generate high-valent $Co^{2+/3+}$;[38] on the other hand, introducing Mo into the electrocatalyst influences the initial electronic structure. Owing to the existence of the element with high electronegativity, Mo provides more electrons instead of partial Co to P ions, which is beneficial for maintaining the low-valent Co^0 and then broadening the valence state range. The Raman spectra of Co_9S_8@$CoMoP_x$ before and after HER were recorded and are shown in Fig. 3g. Typical bands of Co_9S_8 at 468, 515, and 658 cm^{-1} were still retained.[39] In addition, characteristic peaks of MoO_4^{2-} (894 cm^{-1})[37,40–43] and partially oxidized $Co(OH)_x$ (503 and 611 cm^{-1}) appeared after the reaction.[4,43] These further elucidate the coexistence of multivalent metal sites on the surface of Co_9S_8@$CoMoP_x$. Based on the above discussion, the P and S non-metallic elements leach into the electrolyte during the HER process, while OH^- in the alkaline

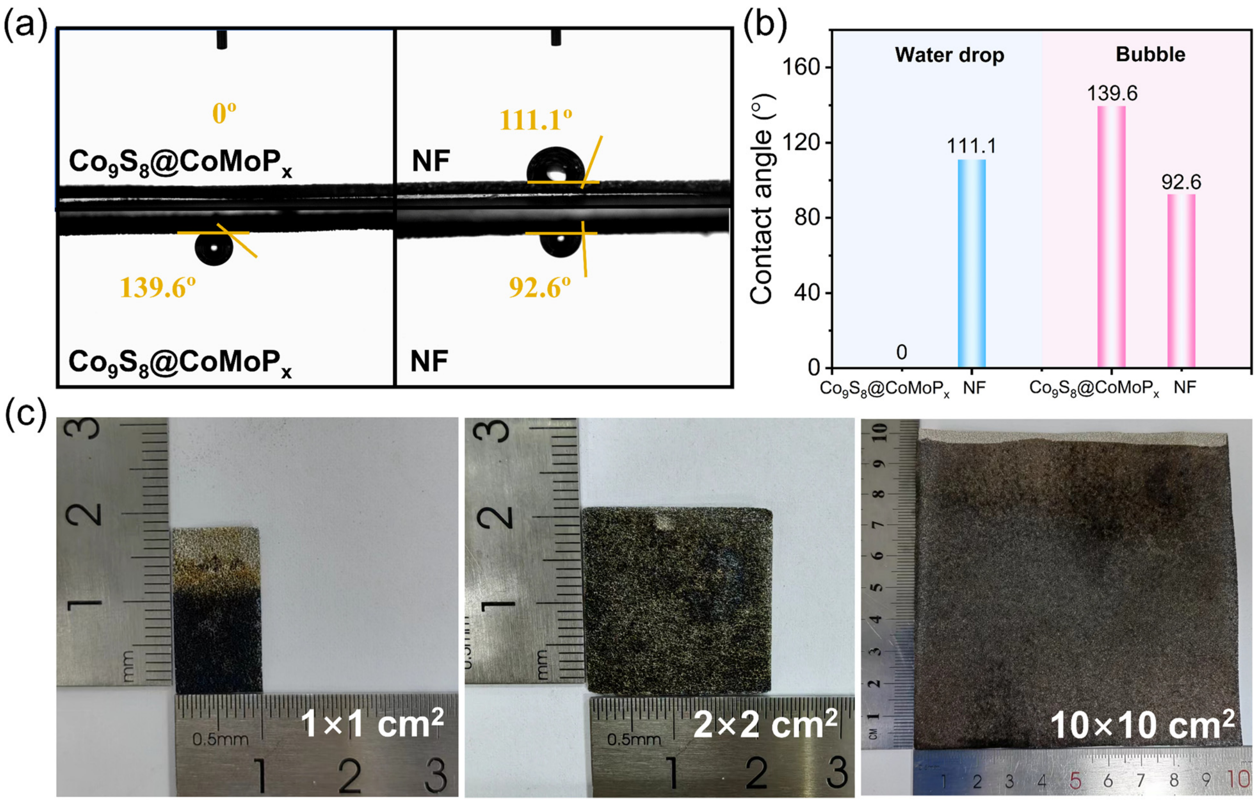

Fig. 4 (a) Static water and bubble contact-angle measurements of the Co_9S_8@$CoMoP_x$ electrocatalyst and blank NF. (b) Comparison diagram of the contact-angle values in Fig. 4a. (c) Scaled-up image of the Co_9S_8@$CoMoP_x$ electrode.

solution attaches on the electrode and affects the valence distribution of metal elements on the surface. Thus, the multivalent states of metal sites with Co^0, $Co^{2+/3+}(Co(OH)_x)$, and $Mo^{6+}(MoO_4{}^{2-})$ coexisted on the electrode surface. The H* in the H_2O molecule can be adsorbed at the low-valent Co^0 sites and OH* is adsorbed at the oxophilic Mo^{6+} metal sites to break the H–OH bond and allow the Volmer step to proceed.[40,44] The H* is subsequently adsorbed at the metal sites with a low-valent state to accomplish the Heyrovsky reaction. In parallel, the presence of $Co(OH)_x$ on the surface can anchor $MoO_4{}^{2-}$ anions,[43] thereby inhibiting the leaching of active sites and improving the catalytic stability of the Co_9S_8@$CoMoP_x$ (Fig. 3h). In conclusion, the multivalent Co element in Co_9S_8@$CoMoP_x$ provides both protophilic low-valence states and oxophilic high-valence states, which is beneficial to accelerate the alkaline HER kinetics with intricate interfacial reactions.

To explore the wettability of the Co_9S_8@$CoMoP_x$ electrode, contact-angle (CA) measurements were then performed, as shown in Fig. 4a and b. The static water contact-angles of Co_9S_8@$CoMoP_x$ and bare NF were 0° and 111.1°, while the bubble contact-angles were 139.6° and 92.6°, respectively. The nearly zero droplet contact-angle and larger bubble contact-angle manifested the hydrophilic property of the Co_9S_8@$CoMoP_x$ surface. This property allows the electrolyte to flow more evenly through the Co_9S_8@$CoMoP_x$ electrode and reduces the "dead zone" during the generation of plentiful hydrogen bubbles.[45,46] Furthermore, the size of the Co_9S_8@$CoMoP_x$ electrode was amplified from 1.0 × 1.0 to 10.0 × 10.0 cm^2 (Fig. 4c), confirming the potential for industrial application of Co_9S_8@$CoMoP_x$ as a cathode.

The self-supported Co_9S_8@$CoMoP_x$ cathode coupled with a Ni_3S_2@$NiFeP_x$ anode was assembled in an alkaline exchange membrane water electrolysis (AEMWE) device to validate its prospects for industrial application (Fig. S23, ESI†).[19] The liquid feeding mode and operating temperature of the device were optimized. According to the polarization curves in Fig. 5a and b, the catalytic activity with a 1.0 mol L^{-1} KOH feed from anodic side delivered the most prominent enhancement because of the increased OH^- concentration at the membrane electrode interface, which accelerated the reaction kinetics and benefitted the release of high-purity hydrogen gas. Moreover, the effect of operation temperature was also explored. As shown in Fig. 5c, the performance of the AEMWE device was enhanced with increasing temperature, as a higher temperature could effectively reduce the R_{ct} of the electrolyser through accelerating the kinetics of charge transfer and the interfacial electrochemical reaction (Fig. 5d). The Co_9S_8@$CoMoP_x$‖Ni_3S_2@$NiFeP_x$-based AEMWE device delivered a current density of 1 A cm^{-2} by applying 1.96 V at 80 °C with the anode feed. The whole electrolyser could stably operate for 30 h under a constant current density of 500 mA cm^{-2} (Fig. 5e) and could be maintained for 10 h during an accelerated attenuation test (Fig. 5f).

Conclusions

In summary, we report a double-layered Co_9S_8@$CoMoP_x$ self-supported electrode with a nanosheet cluster morphology and

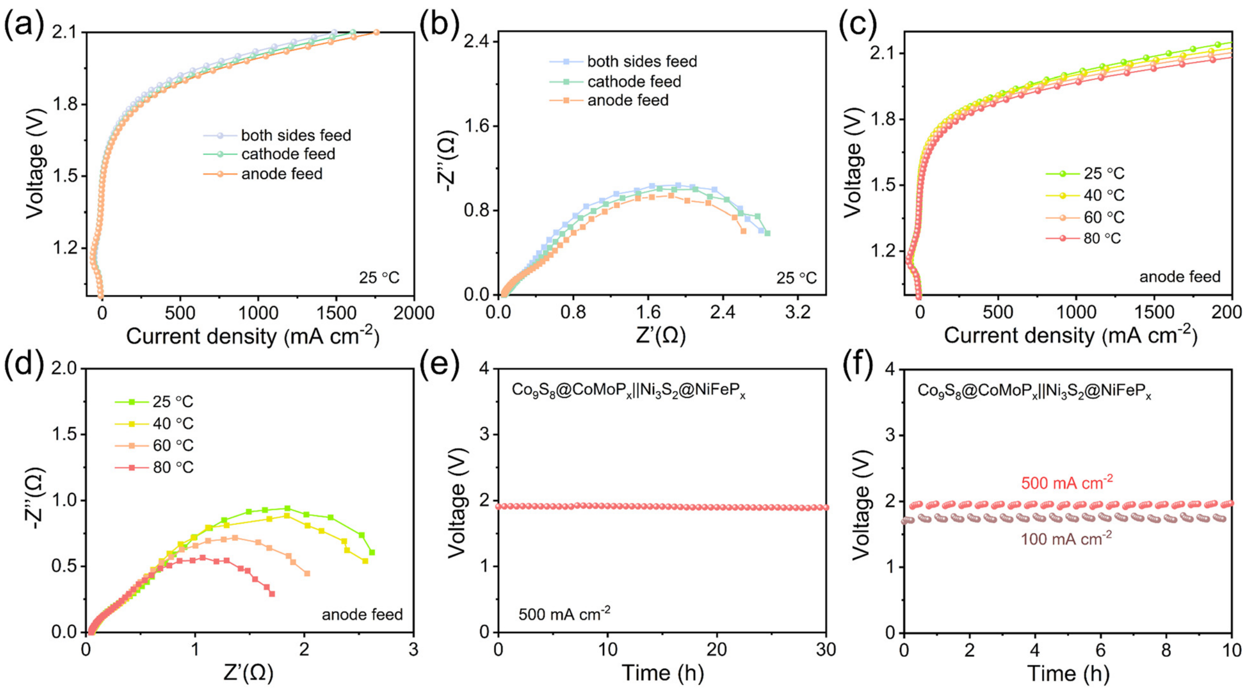

Fig. 5 (a) Polarization curves and (b) Nyquist plots of AEMWE with the Co_9S_8@$CoMoP_x$ cathode at 25 °C in 1.0 mol L^{-1} KOH. (c) Polarization curves and (d) Nyquist plots of Co_9S_8@$CoMoP_x$-based AEMWE with anode feed at different temperatures. (e) Chronopotentiometry curves at 500 mA cm^{-2} and (f) accelerated degradation test of the Co_9S_8@$CoMoP_x$‖Ni_3S_2@$NiFeP_x$-based AEMWE device. An optical picture of the AEMWE device is shown in Fig. S23 (ESI†), and the area sizes of the Co_9S_8@$CoMoP_x$ and Ni_3S_2@$NiFeP_x$ electrodes were both 2 × 2 cm^2.

its electrocatalytic application for hydrogen evolution in AEMWE. The Co_9S_8@$CoMoP_x$ electrocatalyst with the coexistence of multiple metal valence states integrated both oxophilicity and protophilicity properties, exhibiting outstanding HER performance with low overpotentials of 41 and 226 mV at −10 and −500 mA cm^{-2}. Moreover, the $Co(OH)_x$ on the surface could anchor MoO_4^{2-} ions through electrostatic interaction to inhibit Mo leaching, thus enhancing the catalytic stability for long-term operation (1000 h at −500 mA cm^{-2}). In addition, the Co_9S_8@$CoMoP_x$ cathode fabricated by a sequential two-step cathodic electrodeposition was scaled-up and assembled into an AEMWE device coupled with a Ni_3S_2@$NiFeP_x$ anode. This transition metal-based AEMWE device delivered a current density of 1 A cm^{-2} when applying 1.96 V at 80 °C with anode feed. This work highlights the significance of constructing composite electrocatalysts with multivalent metal sites to simultaneously achieve oxophilicity and protophilicity, and also sheds light on designing efficient and stable heterostructure electrodes for energy conversion.

Author contributions

F. C. and X. C. conceived and designed the experiments. X. C. synthesized the catalysts, performed the experiments and data analysis. F. Z. and X. W. assisted the assembly of anion exchange membrane water electrolysis (AEMWE) device. F. L. and J. L. discussed the synthesis of electrocatalysts. M. Y. and F. C. revised the manuscript. All authors discussed the results and contributed to the manuscript.

Data availability

The data supporting this article have been included as part of the ESI† and are available from the authors upon reasonable request.

Conflicts of interest

There are no conflicts to declare.

Acknowledgements

This work was financially supported by the National Key R&D Program of China (No. 2022YFA1504000), the National Natural Science Foundation of China (NSFC, No. 21925503, 22102076, 22121005) and the Fundamental Research Funds for the Central Universities.

References

1 L. Wan, Z. Xu, Q. Xu, M. Pang, D. Lin, J. Liu and B. Wang, *Energy Environ. Sci.*, 2023, **16**, 1384–1430.

2 P. Mardle, B. Chen and S. Holdcroft, *ACS Energy Lett.*, 2023, **8**, 3330–3342.

3 Y. Wang, M. Wang, Y. Yang, D. Kong, C. Meng, D. Zhang, H. Hu and M. Wu, *Chem. Catal.*, 2023, **3**, 100643.

4 K. Zhang, J. Jia, E. Yang, S. Qi, H. Tian, J. Chen, J. Li, Y. Lou and Y. Guo, *Nano Energy*, 2023, **114**, 108601.

5 T. H. Nguyen, P. K. L. Tran, D. T. Tran, V. A. Dinh, N. H. Kim and J. H. Lee, *Appl. Catal., B*, 2024, **343**, 123517.

6 X. Lin, W. Hu, J. Xu, X. Liu, W. Jiang, X. Ma, D. He, Z. Wang, W. Li, L.-M. Yang, H. Zhou and Y. Wu, *J. Am. Chem. Soc.*, 2024, **146**, 4883–4891.

7 G. Gao, G. Zhu, X. Chen, Z. Sun and A. Cabot, *ACS Nano*, 2023, **17**, 20804–20824.

8 X. Guo, X. Wan, Q. Liu, Y. Li, W. Li and J. Shui, *eScience*, 2022, **2**, 304–310.

9 W. Zhang, M. Liu, X. Gu, Y. Shi, Z. Deng and N. Cai, *Chem. Rev.*, 2023, **123**, 7119–7192.

10 X. Chen, X.-T. Wang, J.-B. Le, S.-M. Li, X. Wang, Y.-J. Zhang, P. Radjenovic, Y. Zhao, Y.-H. Wang, X.-M. Lin, J.-C. Dong and J.-F. Li, *Nat. Commun.*, 2023, **14**, 5289.

11 X. Xiao, Z. Li, Y. Xiong and Y.-W. Yang, *J. Am. Chem. Soc.*, 2023, **145**, 16548–16556.

12 X. Wang, G. Long, B. Liu, Z. Li, W. Gao, P. Zhang, H. Zhang, X. Zhou, R. Duan, W. Hu and C. Li, *Angew. Chem., Int. Ed.*, 2023, **62**, e202301562.

13 J. Xu, X. Wang, X. Mao, K. Feng, J. Xu, J. Zhong, L. Wang, N. Han and Y. Li, *Energy Environ. Sci.*, 2023, **16**, 6120–6126.

14 L. Zeng, Z. Zhao, Q. Huang, C. Zhou, W. Chen, K. Wang, M. Li, F. Lin, H. Luo, Y. Gu, L. Li, S. Zhang, F. Lv, G. Lu, M. Luo and S. Guo, *J. Am. Chem. Soc.*, 2023, **145**, 21432–21441.

15 W. Yang, M. Li, B. Zhang, Y. Liu, J. Zi, H. Xiao, X. Liu, J. Lin, H. Zhang, J. Chen, Z. Wan, Z. Li, G. Li, H. Li and Z. Lian, *Adv. Funct. Mater.*, 2023, **33**, 2304852.

16 Y. Liu, T. Sakthivel, F. Hu, Y. Tian, D. Wu, E. H. Ang, H. Liu, S. Guo, S. Peng and Z. Dai, *Adv. Energy Mater.*, 2023, **13**, 2203797.

17 H. Tan, B. Tang, Y. Lu, Q. Ji, L. Lv, H. Duan, N. Li, Y. Wang, S. Feng, Z. Li, C. Wang, F. Hu, Z. Sun and W. Yan, *Nat. Commun.*, 2022, **13**, 2024.

18 J. Li, Z. Xia, Q. Xue, M. Zhang, S. Zhang, H. Xiao, Y. Ma and Y. Qu, *Small*, 2021, **17**, 2103018.

19 X. Chen, K. Xu, J. Li, X. Wang, T. Zhao, F. Liu, M. Yu and F. Cheng, *Chin. Chem. Lett.*, 2023, **34**, 108713.

20 J. Li, F. Liu, M. Yu, H. Hu, H. Liu and F. Cheng, *J. Phys. Chem. C*, 2021, **125**, 25383–25391.

21 N. Yao, G. Wang, H. Jia, J. Yin, H. Cong, S. Chen and W. Luo, *Angew. Chem., Int. Ed.*, 2022, **61**, e202117178.

22 X. Zhu, X. Yao, X. Lang, J. Liu, C. V. Singh, E. Song, Y. Zhu and Q. Jiang, *Adv. Sci.*, 2023, **10**, 2303682.

23 B. Tian, L. Sun and D. Ho, *Adv. Funct. Mater.*, 2023, **33**, 22010298.

24 M. Kim, M. A. R. Anjum, M. Choi, H. Y. Jeong, S. H. Choi, N. Park and J. S. Lee, *Adv. Funct. Mater.*, 2020, **30**, 2002536.

25 S. Qian, F. Xu, Y. Fan, N. Cheng, H. Xue, Y. Yuan, R. Gautier, T. Jiang and J. Tian, *Nat. Commun.*, 2024, **15**, 2774.

26 A. H. Shah, Z. Zhang, C. Wan, S. Wang, A. Zhang, L. Wang, A. N. Alexandrova, Y. Huang and X. Duan, *J. Am. Chem. Soc.*, 2024, **146**, 9623–9630.

27 S. Feng, D. Li, H. Dong, S. Xie, Y. Miao, X. Zhang, B. Gao, P. K. Chu and X. Peng, *Appl. Catal., B*, 2024, **342**, 123451.

28 Z. Chen, W. Gong, J. Wang, S. Hou, G. Yang, C. Zhu, X. Fan, Y. Li, R. Gao and Y. Cui, *Nat. Commun.*, 2023, **14**, 5363.

29 L. Wang, Z. Xu, C. H. Kuo, J. Peng, F. Hu, L. Li, H. Y. Chen, J. Wang and S. Peng, *Angew. Chem., Int. Ed.*, 2023, **62**, e202311937.

30 S. Pan, C. Li, T. Xiong, Y. Xie, F. Luo and Z. Yang, *Appl. Catal., B*, 2024, **341**, 123275.

31 T. Wu, S. Xu, Z. Zhang, M. Luo, R. Wang, Y. Tang, J. Wang and F. Huang, *Adv. Sci.*, 2022, **9**, 2202750.

32 J. Ren, Y. Du, Y. Wang, S. Zhao, B. Yang, B. Li and L. Wang, *Chem. Eng. J.*, 2023, **469**, 143993.

33 Y. Lu, X. Zheng, Y. Liu, J. Zhu, D. Li and D. Jiang, *Inorg. Chem.*, 2022, **61**, 8328–8338.

34 H. Wang, C. Niu, W. Liu and S. Tao, *Appl. Catal., B*, 2024, **340**, 123249.

35 P. Wang, Y. Luo, G. Zhang, M. Wu, Z. Chen, S. Sun and Z. Shi, *Small*, 2021, **18**, 2105803.

36 T. Wu, Y. Sun, X. Ren, J. Wang, J. Song, Y. Pan, Y. Mu, J. Zhang, Q. Cheng, G. Xian, S. Xi, C. Shen, H. J. Gao, A. C. Fisher, M. P. Sherburne, Y. Du, J. W. Ager, J. Gracia, H. Yang, L. Zeng and Z. J. Xu, *Adv. Mater.*, 2022, **35**, 2207041.

37 W. Du, Y. Shi, W. Zhou, Y. Yu and B. Zhang, *Angew. Chem., Int. Ed.*, 2021, **60**, 7051–7055.

38 Y.-N. Zhou, W.-H. Hu, Y.-N. Zhen, B. Dong, Y.-W. Dong, R.-Y. Fan, B. Liu, D.-P. Liu and Y.-M. Chai, *Appl. Catal., B*, 2022, **309**, 121230.

39 J. Gong, W. Luo, Y. Zhao, M. Xie, J. Wang, J. Yang and Y. Dai, *Chem. Eng. J.*, 2022, **434**, 134640.

40 H. Liao, X. Zhang, S. Niu, P. Tan, K. Chen, Y. Liu, G. Wang, M. Liu and J. Pan, *Appl. Catal., B*, 2022, **307**, 121150.

41 X. Tian, R. Ren, F. Wei, J. Pei, Z. Zhuang, L. Zhuang and W. Sheng, *Nat. Commun.*, 2024, **15**, 76.

42 L. Zhou, C. Yang, W. Zhu, R. Li, X. Pang, Y. Zhen, C. Wang, L. Gao, F. Fu, Z. Gao and Y. Liang, *Adv. Energy Mater.*, 2022, **12**, 2202367.

43 L. W. Jiang, Y. Huang, Y. Zou, C. Meng, Y. Xiao, H. Liu and J. J. Wang, *Adv. Energy Mater.*, 2022, **12**, 2202351.

44 J. Greeley, T. Jaramillo, J. Bonde, I. Chorkendorff and J. Nørskov, *Nat. Mater.*, 2006, **5**, 909–913.

45 C. Zhang, Z. Xu, N. Han, Y. Tian, T. Kallio, C. Yu and L. J. Jiang, *Sci. Adv.*, 2023, **9**, eadd6978.

46 M. Li, P. Xie, L. Yu, L. Luo and X. Sun, *ACS Nano*, 2023, **17**, 23299–23316.